

Alma Mater Studiorum Università di Bologna  
Archivio istituzionale della ricerca

An improved 2D arc-star-shaped structure with negative Poisson's ratio: In-plane analysis

This is the final peer-reviewed author's accepted manuscript (postprint) of the following publication:

*Published Version:*

Sindelić V., Nikolić A., Minak G., Bogojević N., Ćirić Kostić S. (2023). An improved 2D arc-star-shaped structure with negative Poisson's ratio: In-plane analysis. MATERIALS TODAY COMMUNICATIONS, 37, 1-12 [10.1016/j.mtcomm.2023.107593].

*Availability:*

This version is available at: <https://hdl.handle.net/11585/955049> since: 2024-11-15

*Published:*

DOI: <http://doi.org/10.1016/j.mtcomm.2023.107593>

*Terms of use:*

Some rights reserved. The terms and conditions for the reuse of this version of the manuscript are specified in the publishing policy. For all terms of use and more information see the publisher's website.

This item was downloaded from IRIS Università di Bologna (<https://cris.unibo.it/>).  
When citing, please refer to the published version.

(Article begins on next page)

# **An improved 2D arc-star-shaped structure with negative Poisson's ratio: in-plane analysis**

Vladimir Sindelić<sup>1</sup>, Aleksandar Nikolić<sup>1\*</sup>, Giangiacomo Minak<sup>2</sup>, Nebojša Bogojević<sup>1</sup>, Snežana Ćirić Kostić<sup>1</sup>

<sup>1</sup> Faculty of Mechanical and Civil Engineering in Kraljevo, University of Kragujevac (Serbia)

<sup>2</sup>Department of Industrial Engineering (DIN), Alma Mater Studiorum—Università di Bologna (Italy)

\*Corresponding author.

E-mail address: nikolic.a@mfkv.kg.ac.rs (A. Nikolić)

## **Abstract**

This paper proposes an improved 2D arc-star-shaped structure with a negative Poisson's ratio, whereas the analytical and finite element analyses were performed. Furthermore, the model of the improved 2D arc-star-shaped structure was produced by using selective laser sintering additive technology and scanned after that by using the optical measurement technique on the ATOS COMPACT SCAN 5M scanner to obtain experimental measurements. It has been observed that for the same geometric parameters, a higher value of the negative Poisson's ratio is obtained compared to the initial 2D arc-star structure with the most often lower value of relative density, which directly leads to lower consumption of the material.

**Keywords:** Arc-star-shaped structure; Negative Poisson's ratio; Auxetic; Metamaterials; Selective laser sintering; Optical measurement technique

# 1. Introduction

Poisson's ratio is defined as the ratio of transverse and axial material deformations under the action of axial static forces. In the case of bulk-form of the materials, the value of Poisson's ratio is positive. However, the industry's need for ultra-lightweight structures has led to the emergence of a new group of artificially designed materials known as mechanical metamaterials. These materials, in addition to forming an ultra-light structure, can provide the same, better, or give some new properties to the structure with their design. Additive manufacturing has a special and significant role in the creation and development of mechanical metamaterials. The development of these technologies allowed designers great freedom when constructing structures. The possibility to assign some new properties to ultra-light structures has led to the emergence of a new group of metamaterials that have a negative Poisson's ratio (NPR in the further). Mechanical metamaterials with NPR, have the main character that under the effect of axial static pressure forces, they have transverse shrinkage. Because of this characteristic, they have a very good ability to absorb energy, so they are widely used in various branches of industry such as the aviation industry, the space industry, biomedicine, the sports industry, etc. Mechanical metamaterials with NPR consist of an "auxetic" structure. First of all, there were different forms of auxetic honeycomb structures [1–6]. Since then, there have been many researches, analytical, numerical, or experimental, in which the redesign of the auxetic structure of the honeycomb is carried out to increase the value of NPR or energy absorption capacity [7–29].

In addition to the auxetic honeycomb structures, other structures can provide us with NPR due to their shape. An example of such a structure is a star-shaped structure which, due to its shape, provides NPR values in both vertical and horizontal directions. In references [30–32], various shapes of star structures were made by using additive manufacturing, and then their mechanical properties and NPR values were examined. Jin et al. [33] studied the mechanical properties of a structure obtained by combining star and auxetic honeycomb structures. Liu et al. [34] proposed a novel star-shaped cellular structure with great elastic properties as a candidate for multiple morphing applications. Ai and Gao [35] developed a new analytical model for three types of 2D periodic star-shaped auxetic structures that possess orthotropic symmetry and exhibit NPR. Li et al. [36] proposed a novel 2D metamaterials with variable values of NPR as well as with negative thermal expansion. Zhang et al. [37] analyzed a new 2D arc-

star structure (2D-AS in the further) analytically, numerically, and experimentally, based on the traditional star structure, which can achieve negative, zero, and positive values of Poisson's ratio.

This research is based on 2D-AS [37], to obtain higher NPR values while consuming less material by modifying the structure's geometry. The goal is to initially establish a relation between the geometric parameters of 2D-AS and its improved version (*i*2D-AS in the further). After that, an analytical model will be formed to obtain Poisson's ratio. The established analytical model will be verified by applying the finite element method (FEM in the further) as well as deformation measurements on the real model obtained by selective laser sintering technology (SLS in the further). Finally, it is interesting to compare the NPR values of 2D-AS and *i*2D-AS to judge whether the proposed changes to the 2D-AS geometry gave the desired result.

## 2. Design of the improved 2D-AS structure

Figure 1(a-c) describes the idea of the redesign of the representative volume element (RVE in the further) of the 2D-AS structure. Namely, the original RVE of the 2D-AS structure shown in Fig. 1(a) was modified by removing the straight parts of the structure as well as the part of the arc of radius  $r$ , both painted in red on Fig. 1(b) and at the same time replaced it with the black colored arc shown in the same figure. As a result, the RVE of the *i*2D-AS structure shown in Fig. 1(c) was obtained.

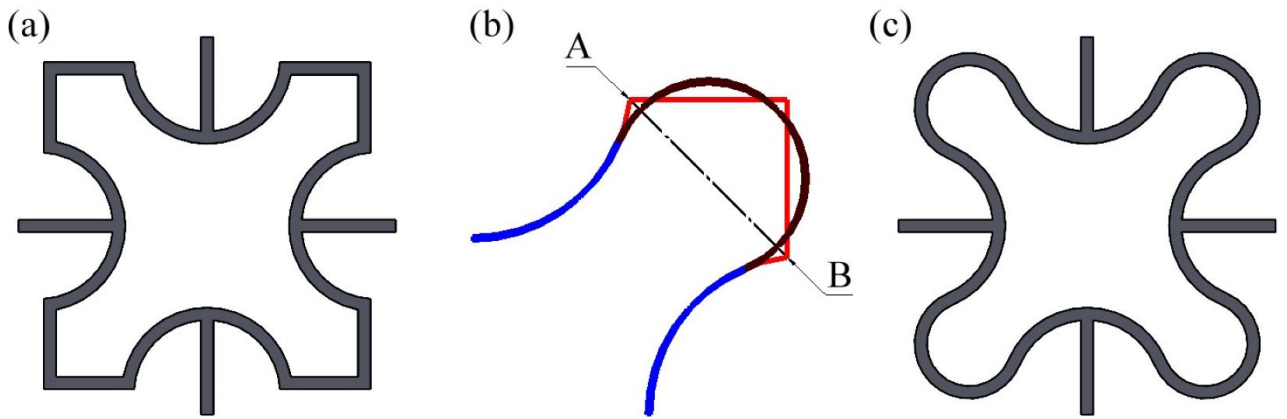


**Fig. 1.** RVE: (a) 2D-AS [37]; (b) The redesign of the 2D-AS; (c) *i*2D-AS.

The following geometric parameters are common for both RVE of the structures, 2D-AS and *i*2D-AS (see Fig. 2): the length  $L$ , the height  $h$ , depth  $d$ , the thickness  $t$ , the arc radius  $r$ , the arc angle  $\theta$ , the total length of the structure

along the horizontal and vertical direction  $L_x$  and  $L_y$ , respectively, as well as the coefficients  $a$  and  $b$  that must satisfy the following conditions  $0 < a < 1$  and  $0 < b < 1$ .

Moreover, the parameters  $\theta$  and  $r$  are defined in reference [37] as follows:

$$\theta = 2 \arctan \frac{bh}{ah}, \quad (1)$$

$$r = \frac{ah}{\sin \theta}. \quad (2)$$

In addition to the mentioned common parameters, for the description of the RVE of the *i*2D-AS structure it is necessary to introduce some new parameters shown in Figs. 2(b) and (c): the arc of the new radius  $R$ , the arc angle  $\psi$  of the truncated radius  $r$ , the angle  $\varphi$  representing the difference between the old angle  $\theta$  and the new angle  $\psi$  of radius  $r$ , as well as the angle  $\alpha$  formed by the lines DE and AE.

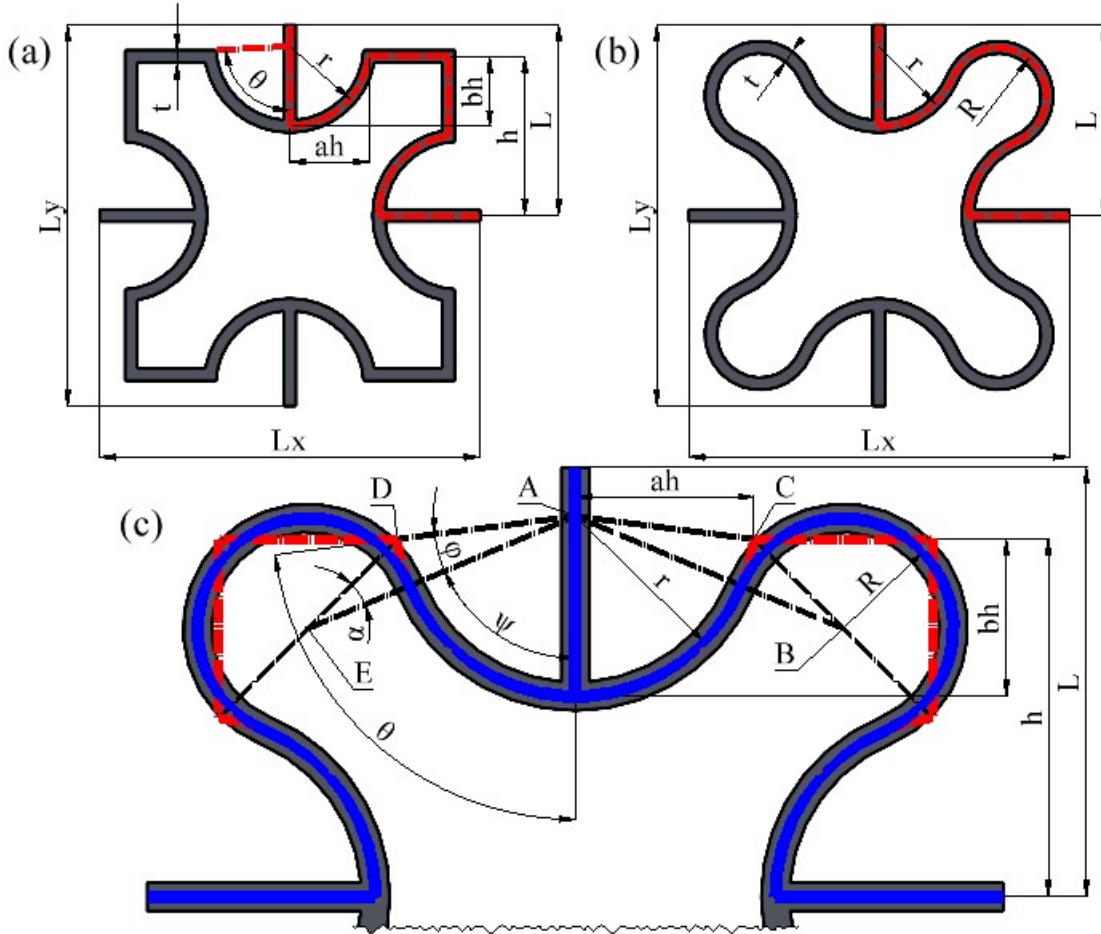


**Fig. 2.** Geometric parameters of the RVE: (a) 2D-AS [37]; (b) *i*2D-AS; (c) detailed view of the *i*2D-AS.

Looking at the triangle AED in Fig. 2(c), first by projecting the side AE onto the horizontal direction, we obtain:

$$(R+r)\sin(\theta-\varphi) = \frac{h+ah}{2}. \quad (3)$$

Also, applying the sine theorem to this triangle yields:

$$\frac{r}{\sin \alpha} = \frac{\sqrt{2}(h-ah)}{2 \cdot \sin \varphi} = \frac{R+r}{\sin(\pi-\varphi-\alpha)}. \quad (4)$$

By solving the previous two equations, the unknown parameters  $R$ ,  $\varphi$ , and  $\alpha$  can be expressed as a function of the above-defined parameters. Due to the existence of trigonometric functions, these dependencies are not easy to show explicitly in symbolic form, but they can be determined later in numerical examples by specifying numerical values of the input parameters  $h$ ,  $ah$ , and  $bh$ .

Finally, let's note that the angle  $\psi$  can be obtained by subtracting the angle  $\varphi$  from the angle  $\theta$ :

$$\psi = \theta - \varphi. \quad (5)$$

Based on all previously defined geometric parameters, the relative density of the *i*2D-AS can be determined as follows:

$$\rho_r = (L - h + bh + (\pi + 2\alpha)R + 2r\psi) \frac{t}{L^2}. \quad (6)$$

### 3. Poisson's ratio of the *i*2D-AS

#### 3.1 Analytical model

To study the Poisson's ratio of *i*2D-AS, it is sufficient to analyze its RVE, which is extracted from the structure as shown in Fig. 3.

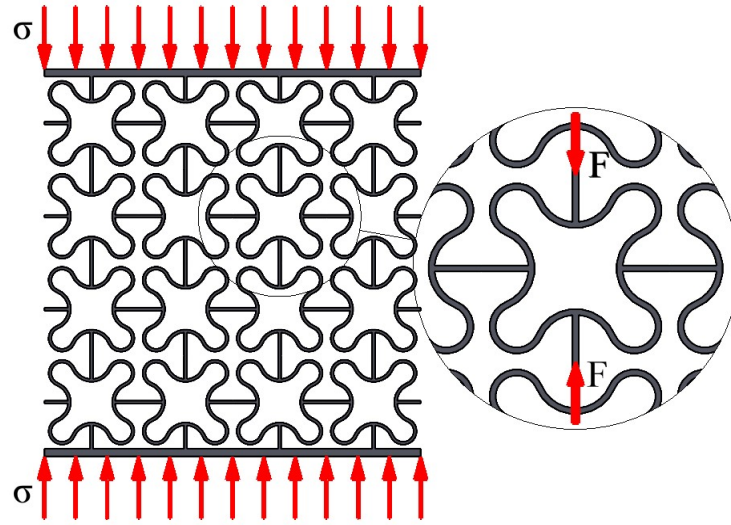


**Fig. 3.** Extracting of RVE from the *i2D-AS*.

The following assumptions of RVE will be used when creating the analytical model: the deformations are small so they belong to the elastic area, the thickness of RVE is much smaller compared to its length, and the RVE is a part of an infinite structure so there is no need for considering boundary effect.

Due to the symmetry of the load and the RVE itself, further analysis can be carried out on the half of the RVE, as it is shown in Fig. 4.

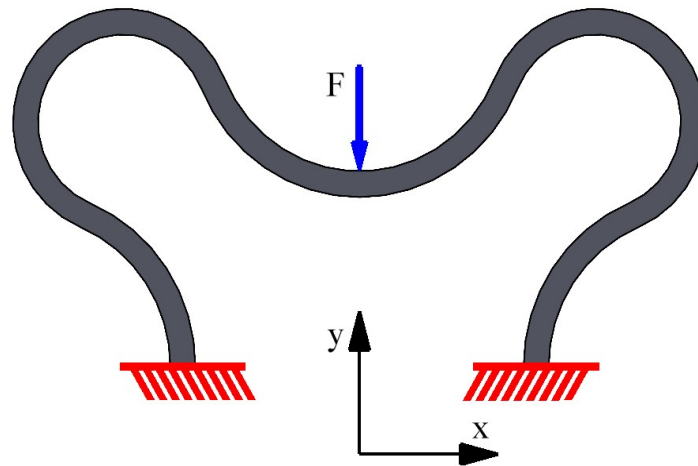


**Fig. 4.** The half of the RVE from the *i2D-AS*.

Now, the previously presented half of the RVE was divided into two quarters, left and right, as shown in Fig. 5. The influence of the left quarter of the RVE on the right one, and vice versa, is described by the internal reaction

forces  $Y_O$  and  $Y_O'$  and reaction couple of moments  $M_O$  and  $M_O'$  which occur in pairs and have the same intensity but opposite directions.

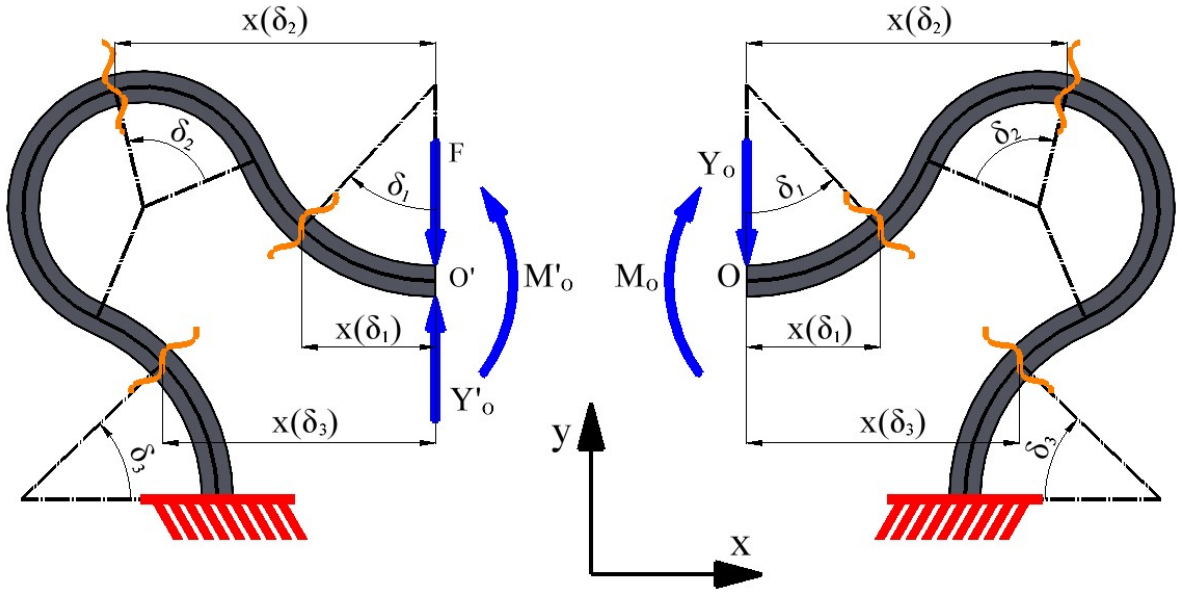


**Fig. 5.** Dividing one-half of the RVE of the *i2D-AS* into two quarters.

The values of reaction force  $Y_O$  and a couple of moments  $M_O$  can be determined from the condition that the vertical displacement, as well as the angle of rotation of points  $O$  and  $O'$ , are equal, so by applying Castigliano's second theorem, we get :

$$\frac{\partial U}{\partial Y_O} + \frac{\partial U}{\partial Y_O'} = \frac{1}{EI} \sum_{i=1}^3 \int_0^{\varphi_i} \left( M_i \frac{\partial M_i}{\partial Y_O} + M_i' \frac{\partial M_i'}{\partial Y_O} \right) r_i d\delta_i = 0, \quad (7)$$

$$\frac{\partial U}{\partial M_O} + \frac{\partial U}{\partial M_O'} = \frac{1}{EI} \sum_{i=1}^3 \int_0^{\varphi_i} \left( M_i \frac{\partial M_i}{\partial M_O} + M_i' \frac{\partial M_i'}{\partial M_O} \right) r_i d\delta_i = 0, \quad (8)$$

where  $E$  is Young's modulus,  $I$  represents the RVE cross-section moment of inertia,

$$\varphi_i = \begin{cases} \psi, & i = 1, 3 \\ 2\alpha + \pi, & i = 2 \end{cases} \quad (9)$$

represents the final values of angles  $\delta_i$ , and



$$r_i = \begin{cases} r, & i = 1, 3 \\ R, & i = 2 \end{cases} \quad (10)$$

is the radius of the three introduced fields.

Bending moments in all of the introduced fields can be determined as:

$$M_i = M_O - Y_O \cdot x(\delta_i), \quad (11)$$

$$M_i' = M_O' + (Y_O' - F) \cdot x(\delta_i), \quad i = 1, 2, 3, \quad (12)$$

where:

$$x(\delta_1) = r \cdot \sin \delta_1, \quad (13)$$

$$x(\delta_2) = (r + R) \cdot \sin \psi - R \cdot \cos \left( \frac{\pi}{2} - \psi + \delta_2 \right), \quad (14)$$

$$x(\delta_3) = (r + R) \cdot \sin \psi + (r + R) \cdot \cos \psi - r \cdot \cos \delta_3. \quad (15)$$

By substituting the expressions (9-15) into equations (7) and (8) and solving for the unknowns  $Y_O$  and  $M_O$ , we get:

$$Y_O = \frac{F}{2}, \quad (16)$$

$$M_O = \frac{F}{2\pi R + 4R\alpha + 4r\psi} \left( \begin{aligned} & r^2 + 2R^2 \cos \alpha \cdot \cos(\alpha - \psi) + r(r(\psi - 1) + R\psi) \cos \psi \\ & + (-r^2 + \pi r R + \pi R^2 + 2rR\alpha + 2R^2\alpha + r^2\psi + rR\psi) \sin \psi \end{aligned} \right). \quad (17)$$

Since the values of the reactions  $Y_O$  and  $M_O$  have now been determined, when calculating the displacement of point O only a quarter of the RVE can be observed. Here, the right quarter of the RVE from the Fig. 5 is selected.

By doing this, only the downward vertical force  $Y_O$ , along with the moment  $M_O$ , now acts at point O, as shown in Fig. 6. Furthermore, a fictitious force  $X_O=0$  is introduced at point O to simplify the determination of its horizontal displacement by using the Castigliano's second theorem.

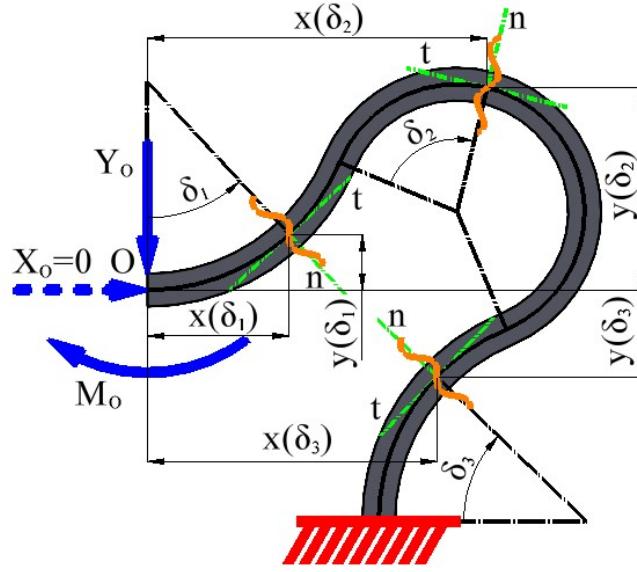


**Fig. 6.** The horizontal and vertical displacement of the point O of the *i*2D-AS.

Now, the horizontal and vertical displacement of point O should be obtained as:

$$f_x = \sum_{i=1}^3 \int_0^{\delta_i} \left( \frac{1}{EI} M_i \cdot \frac{\partial M_i}{\partial X_o} + \frac{1}{EA} N_i \frac{\partial N_i}{\partial X_o} + \frac{k}{GA} T_i \frac{\partial T_i}{\partial X_o} \right) r_i d\delta_i, \quad (18)$$

$$f_y = \sum_{i=1}^3 \int_0^{\delta_i} \left( \frac{1}{EI} M_i \cdot \frac{\partial M_i}{\partial Y_o} + \frac{1}{EA} N_i \frac{\partial N_i}{\partial Y_o} + \frac{k}{GA} T_i \frac{\partial T_i}{\partial Y_o} \right) r_i d\delta_i, \quad (19)$$

where

$$G = \frac{E}{2(1+\nu_m)} \quad (20)$$

is shear modulus,  $\nu_m$  is Poisson's ratio of the bulk-form of the material of the RVE,

$$A = td, \text{ and } I = \frac{td^3}{12} \quad (21)$$

represent the area and moment of inertial of the RVE cross-section, respectively, and  $k$  is the shear coefficient.

Bending moments in all of the three introduced fields shown in Fig. 6 can be determined as:

$$M_i = M_o - Y_o \cdot x(\delta_i) - X_o \cdot y(\delta_i), \quad i = 1, 2, 3, \quad (22)$$

where

$$y(\delta_1) = r - r \cdot \cos(\delta_1), \quad (23)$$

$$y(\delta_2) = r - (r + R) \cdot \cos(\psi) + R \cdot \sin\left(\frac{\pi}{2} - \psi + \delta_2\right), \quad (24)$$

$$y(\delta_3) = (r + R) \cdot \sin(\psi) - (r - (r + R) \cdot \cos(\psi)) - r \cdot \sin(\delta_3). \quad (25)$$

Note that values  $x(\delta_i)$  ( $i=1,2,3$ ) are determined above, in equations (13-15).

Axial and transverse forces in all introduced fields were obtained by projecting the forces onto the tangent and normal directions, respectively, so they read:

$$N_1 = -X_o \cdot \cos(\delta_1) - Y_o \cdot \sin(\delta_1), \quad (26)$$

$$N_2 = -X_o \cdot \cos(\psi - \delta_2) + Y_o \cdot \sin(\psi - \delta_2), \quad (27)$$

$$N_3 = X_o \cdot \sin(\delta_3) - Y_o \cdot \cos(\delta_3), \quad (28)$$

$$T_1 = -X_o \cdot \sin(\delta_1) - Y_o \cdot \cos(\delta_1), \quad (29)$$

$$T_2 = -X_o \cdot \sin(\psi - \delta_2) - Y_o \cdot \cos(\psi - \delta_2), \quad (30)$$

$$T_3 = X_o \cdot \cos(\delta_3) + Y_o \cdot \sin(\delta_3). \quad (31)$$

Note that after calculating the integrals (18) and (19), it should be taken into account that  $X_o=0$ , and that the vertical reaction force  $Y_o$  and the reaction couple of moment  $M_o$  are given by the expressions (16) and (17), respectively.

Finally, the Poisson's ratio of the observed RVE can be determined by using the following expression [37]:

$$\nu = -\frac{\varepsilon_x}{\varepsilon_y} = -\frac{f_x}{f_y} \cdot \frac{L_y}{L_x}. \quad (32)$$

### 3.1.1 Numerical example

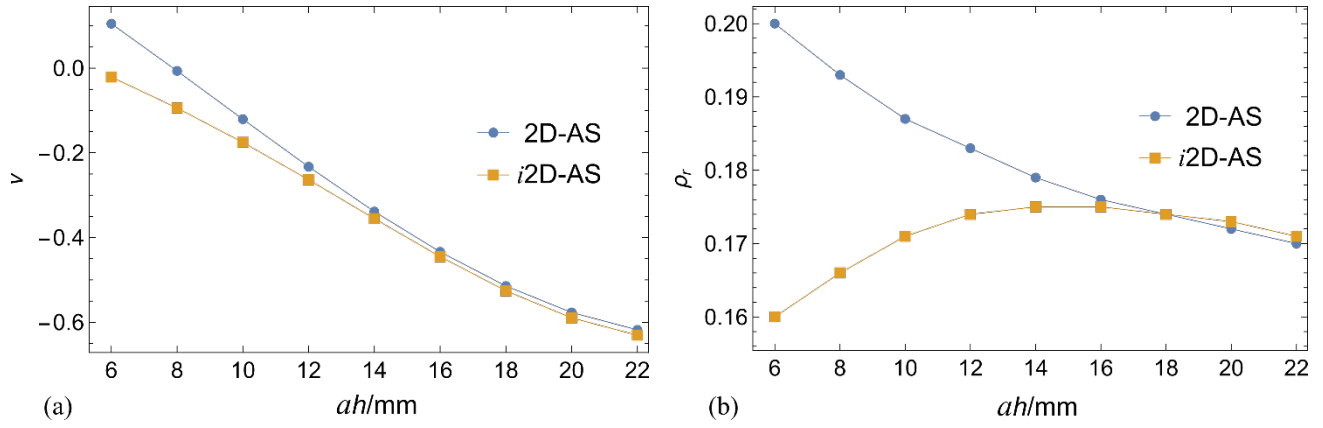
This example will consider a comparison of the values of the Poisson's ratio  $\nu$  and relative density  $\rho_r$  of 2D-AS and *i*2D-AS for various values of geometric parameters  $ah$  and  $bh$ . From now on, the following numerical values of the geometric and material parameters will be used:  $L=30$  mm,  $h=25$  mm,  $t=2$  mm,  $d=3$  mm, and  $\nu_m=0.4$ .

Table 1 shows the values of the  $\nu$  and  $\rho_r$  of the 2D-AS and *i*2D-AS whereas the value of the parameter  $bh$  is fixed at 12.5 mm and the value of parameter  $ah$  increases from 6 mm to 22 mm with step equal to 2 mm. All values of NPR of the *i*2D-AS are higher relative to the corresponding ones of the 2D-AS. What is particularly important to emphasize is that the relative densities  $\rho_r$  of *i*2D-AS are lower relative to those of 2D-AS for  $ah=6$  mm up to  $ah=18$  mm where these values are equal for both structures. Therefore, from  $ah=6$  mm to  $ah=22$  mm, *i*2D-AS gives higher values of NPR, while the relative density is lower compared to 2D-AS. The lower value of relative density leads to a lighter structure and less material is needed for its production. For values of  $ah$  greater than 18mm, 2D-AS has a slightly lower relative density relative to *i*2D-AS, although the value of the NPR of *i*2D-AS is still slightly higher.

A graphical presentation of the dependence of Poisson's ratio  $\nu$  and relative density  $\rho_r$  on  $ah$  for 2D-AS and *i*2D-AS is shown in Fig. 7.

**Table 1.**  
Dependence of  $\nu$  and  $\rho_r$  on the parameter  $ah$  of 2D-AS and *i*2D-AS.

| $ah/\text{mm}$ |                | 6       | 8       | 10      | 12      | 14      | 16      | 18      | 20      | 22      |
|----------------|----------------|---------|---------|---------|---------|---------|---------|---------|---------|---------|
| $\nu$          | 2D-AS          | 0.1051  | -0.0065 | -0.1205 | -0.2328 | -0.3387 | -0.4339 | -0.5145 | -0.5770 | -0.6181 |
|                | <i>i</i> 2D-AS | -0.0208 | -0.0941 | -0.1753 | -0.2635 | -0.3553 | -0.4451 | -0.5258 | -0.5898 | -0.6307 |
| $\rho_r$       | 2D-AS          | 0.2001  | 0.1929  | 0.1872  | 0.1827  | 0.1791  | 0.1761  | 0.1736  | 0.1716  | 0.1698  |
|                | <i>i</i> 2D-AS | 0.1605  | 0.1664  | 0.1708  | 0.1735  | 0.1748  | 0.1750  | 0.1742  | 0.1727  | 0.1709  |



**Fig. 7.** Comparison of the 2D-AS and *i*2D-AS dependence on parameter  $ah$  for: (a) Poisson's ratio  $\nu$ , (b) relative density  $\rho_r$ .

Table 2 shows the values of the  $\nu$  and  $\rho_r$  of the 2D-AS and *i*2D-AS whereas the value of the parameter  $ah$  is fixed at 12.5 mm and the value of parameter  $bh$  increases from 6 mm to 16 mm with step equal to 2 mm. Here, too, the value of the Poisson's ratio  $\nu$  of the *i*2D-AS is higher than 2D-AS for each value of  $bh$ . Also, the relative density  $\rho_r$  of the *i*2D-AS is lower for  $bh$  from 10 to 16 mm, but it is higher for  $bh$  from 6 to 8 mm. A graphical representation of the dependence of Poisson's ratio  $\nu$  and relative density  $\rho_r$  on parameter  $bh$  for 2D-AS and *i*2D-AS is shown in Fig. 8.

**Table 2.**  
Dependence of  $\nu$  and  $\rho_r$  on the parameter  $bh$  of 2D-AS and *i*2D-AS.

| $bh/\text{mm}$ |                | 6      | 8      | 10      | 12      | 14      | 16      |
|----------------|----------------|--------|--------|---------|---------|---------|---------|
| $\nu$          | 2D-AS          | 0.2180 | 0.0766 | -0.0717 | -0.2226 | -0.3690 | -0.5008 |
|                | <i>i</i> 2D-AS | 0.1711 | 0.0439 | -0.0942 | -0.2462 | -0.4095 | -0.5738 |
| $\rho_r$       | 2D-AS          | 0.1437 | 0.1541 | 0.1657  | 0.1784  | 0.1919  | 0.2062  |
|                | <i>i</i> 2D-AS | 0.1496 | 0.1576 | 0.1650  | 0.1722  | 0.1794  | 0.1868  |

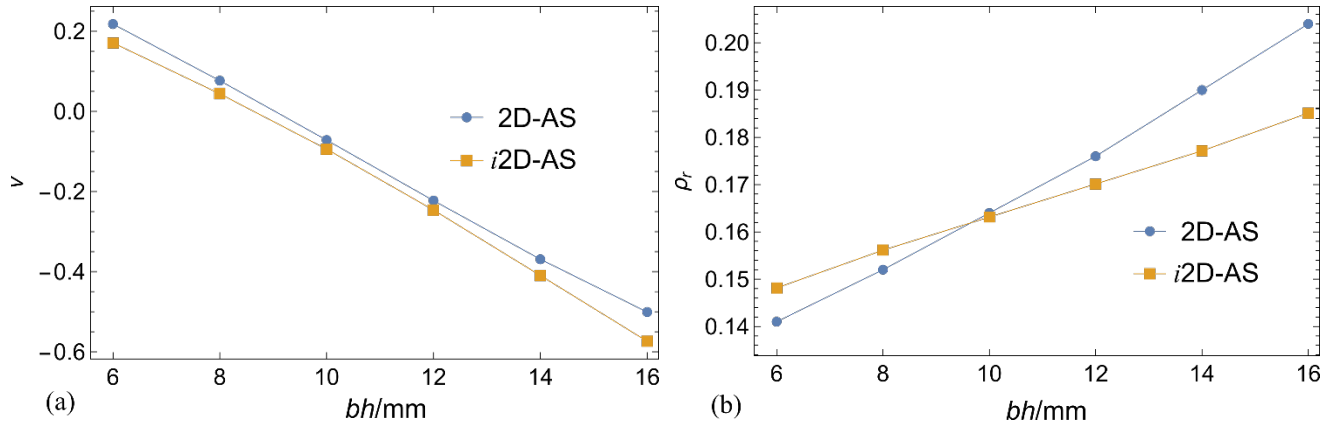


**Fig. 8.** Dependence of 2D-AS and i2D-AS on parameter  $bh$  for: (a) Poisson's ratio  $\nu$ , (b) relative density  $\rho_r$ .

A better insight into the dependence of Poisson's ratio  $\nu$  and relative density  $\rho_r$  on the parameters  $ah$  and  $bh$  of i2D-AS can be obtained by observing the 3D graphs shown in Figure 9 (a) and (b), respectively. As the value of parameters  $ah$  and/or  $bh$  increases, so does the value of NPR. The situation is somewhat different with relative density  $\rho_r$ . With the increase of the parameter  $bh$ , at any value  $ah$ , the relative density  $\rho_r$  increases monotonically. On the other hand, at any value of  $bh$ , up to some value of  $ah$ , the value of relative density increases. After that, it decreases. The position of the extreme value of the curve, in which the relative density begins to decrease even though the parameter  $ah$  continues to increase, is different for each  $bh$ .

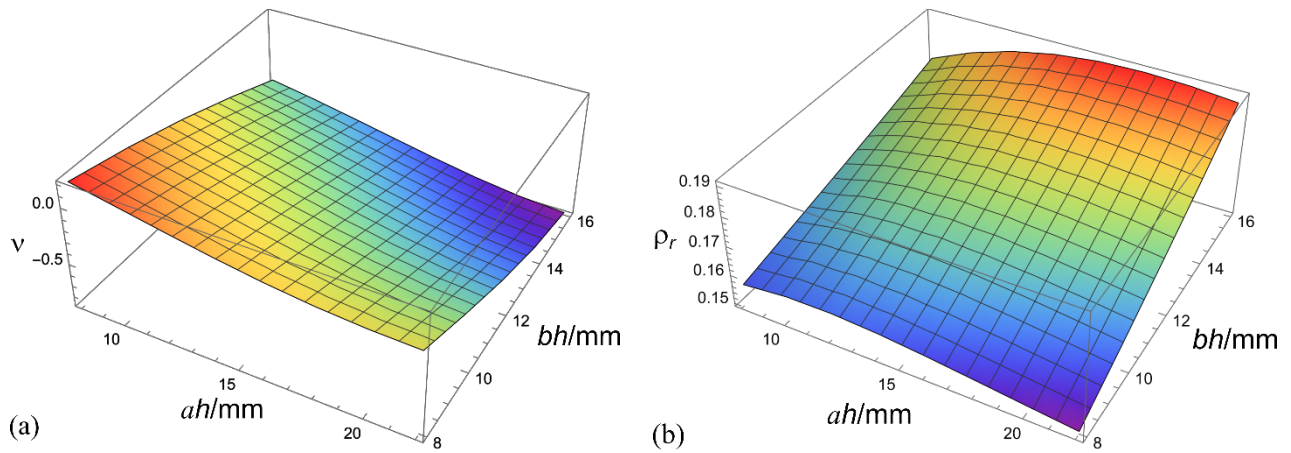


**Fig. 9.** i2D-AS: (a) dependence of  $\nu$  on the parameters  $ah$  and  $bh$ , (b) dependence of  $\rho_r$  on the parameters  $ah$  and  $bh$ .

### 3.2 Finite element method

Here will be performed displacement and stress analysis of the *i*2D-AS by using the FEM in the ANSYS software. All of the geometric parameters of the structure are the same as in the previous numerical example. It was assumed that the material of the structure is polyamide 12 with Young's modulus  $E=1500$  MPa and density  $\rho=0.92$  g/cm<sup>3</sup>. The FE mesh contains mainly Hex20 - 20 node hexahedral elements and some 15 node tetrahedral - Wed 15 elements with a maximal element size of 0.2 mm.

Figure 10 shows the deformation plan, to indirectly determine the Poisson's ratio  $\nu$  of the observed RVE by using the expression (32). It is assumed that the RVE is clamped to a stationary base at point A and that at point B the vertical displacement  $f_y=3$  mm is given. By following the change in the position of points C and D into the C' and D', the horizontal deformation  $f_x$  of the entire structure was obtained, as shown in Fig. 10.

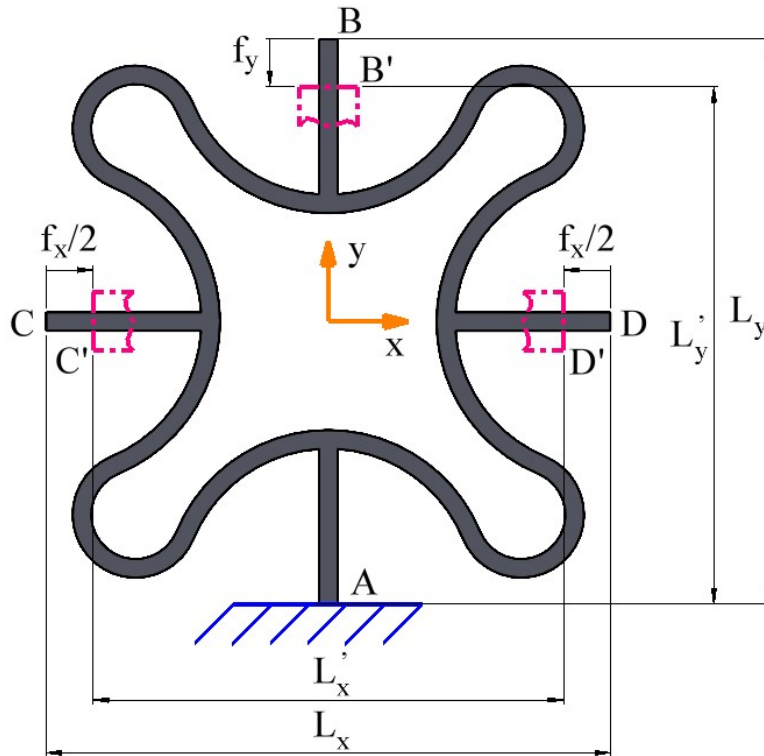


**Fig. 10.** Deformation plan of the RVE of *i*2D-AS

Figure 11 (a-d) shows the deformed *i*2D-AS for the various values of parameter  $ah$ , while Fig. 12 shows the deformed *i*2D-AS for various parameter  $bh$ . By analyzing these figures, it can be concluded that for the same

value of the specified vertical displacement  $f_y=3$  mm, with an increase the value of the parameters  $ah$  and/or  $bh$ , the higher values of the horizontal displacement  $f_x$  occur.

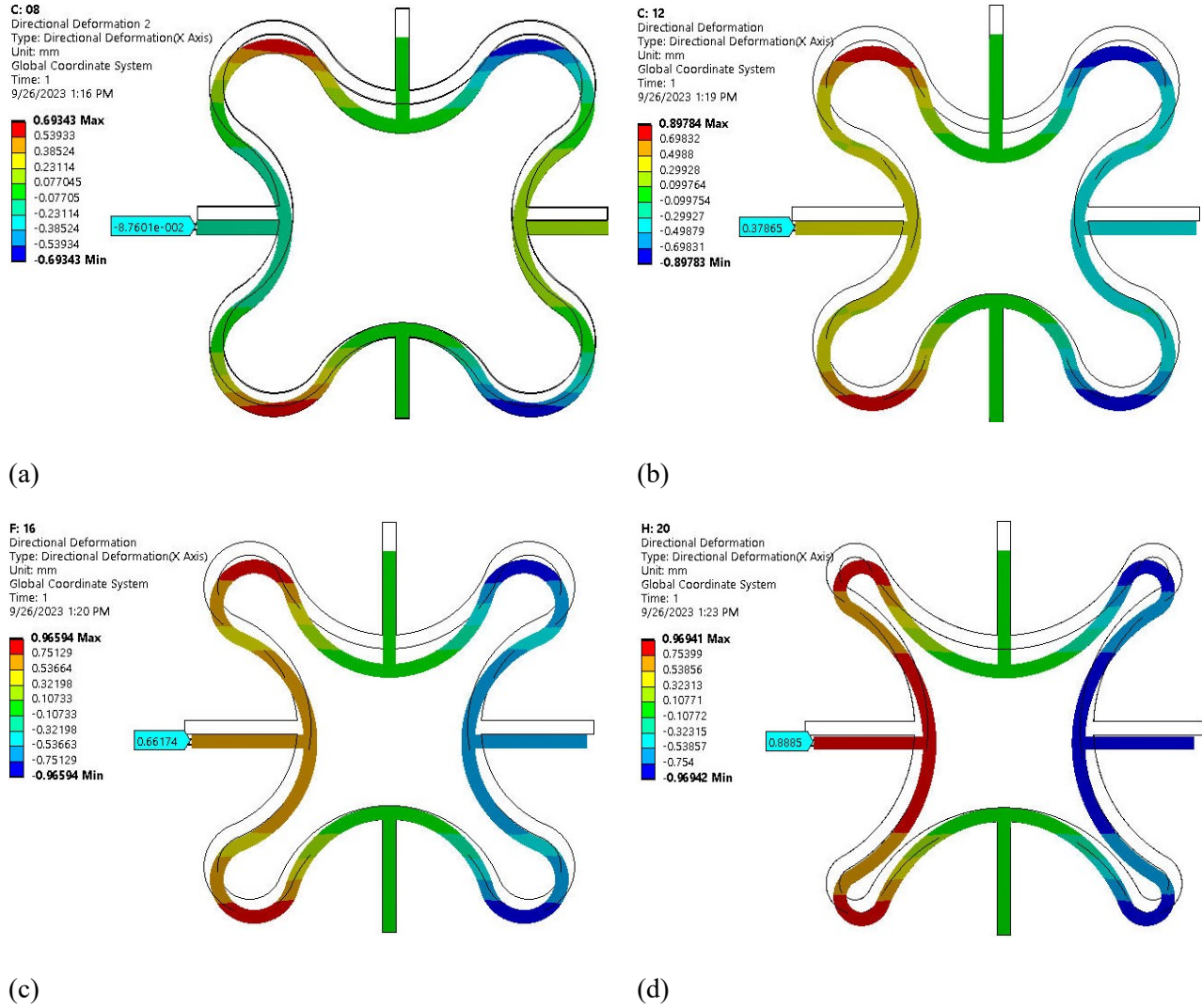


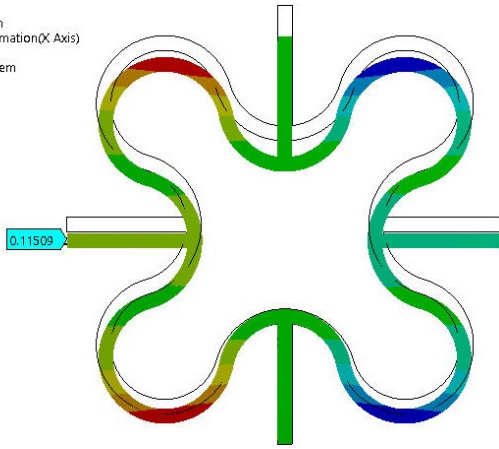
**Fig. 11.** Plane deformation of *i2D-AS* for various values of parameter  $ah$  and  $bh=12.5$  mm:

(a)  $ah=8$  mm, (b)  $ah=12$  mm, (c)  $ah=16$  mm, (d)  $ah=20$ mm.



**A: 8**  
 Directional Deformation  
 Type: Directional Deformation(X Axis)  
 Unit: mm  
 Global Coordinate System  
 Time: 1  
 9/26/2023 1:18 PM

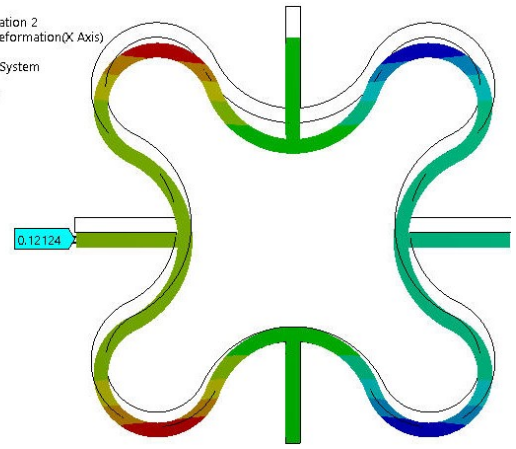
**0.80586 Max**  
 0.62678  
 0.4477  
 0.26861  
 0.089532  
 -0.08955  
 -0.26863  
 -0.44772  
 -0.6268  
**-0.80588 Min**



(a)

**E: 10**  
 Directional Deformation 2  
 Type: Directional Deformation(X Axis)  
 Unit: mm  
 Global Coordinate System  
 Time: 1  
 9/26/2023 1:15 PM

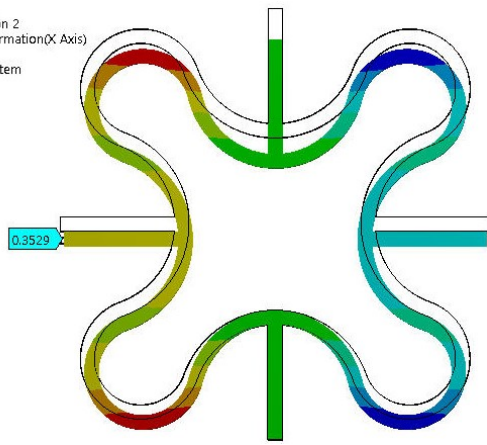
**0.793 Max**  
 0.61678  
 0.44055  
 0.26433  
 0.088111  
 -0.08811  
 -0.26433  
 -0.44055  
 -0.61677  
**-0.79299 Min**



(b)

**A: 12**  
 Directional Deformation 2  
 Type: Directional Deformation(X Axis)  
 Unit: mm  
 Global Coordinate System  
 Time: 1  
 9/26/2023 1:13 PM

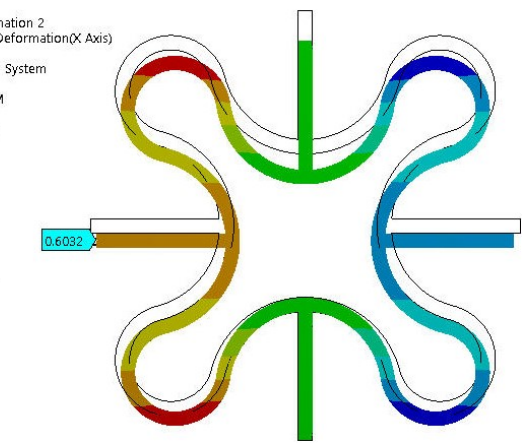
**0.88687 Max**  
 0.68979  
 0.49271  
 0.29563  
 0.098545  
 -0.098536  
 -0.29562  
 -0.4927  
 -0.68978  
**-0.88686 Min**



(c)

**C: 14**  
 Directional Deformation 2  
 Type: Directional Deformation(X Axis)  
 Unit: mm  
 Global Coordinate System  
 Time: 1  
 9/26/2023 1:06 PM

**0.96483 Max**  
 0.75042  
 0.53602  
 0.32161  
 0.1072  
 -0.10721  
 -0.32162  
 -0.53602  
 -0.75043  
**-0.96484 Min**



(d)

**Fig. 12.** Plane deformation of *i2D-AS* for various values of parameter  $bh$  and  $ah=12.5$  mm:

(a)  $bh=8$  mm, (b)  $bh=10$  mm, (c)  $bh=12$  mm, (d)  $bh=14$ mm.

The comparison of the obtained values of Poisson's ratio  $\nu$  by FEM and the analytical results for the various values of parameters  $ah$  and  $bh$  are shown in Table 3. A satisfactory match of the results can be observed.

**Table 3.**

The values of the Poisson's ratio  $\nu$  of *i*2D-AS obtained by the analytical model and FEM for various values of the parameters  $ah$  and  $bh$ .

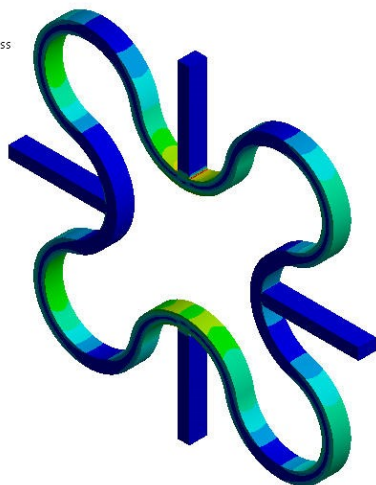
|       | Method     | $ah/\text{mm}$ ( $bh=12.5\text{mm}$ ) |         |         |         | $bh/\text{mm}$ ( $ah=12.5\text{mm}$ ) |         |         |         |
|-------|------------|---------------------------------------|---------|---------|---------|---------------------------------------|---------|---------|---------|
|       |            | 8                                     | 12      | 16      | 20      | 8                                     | 10      | 12      | 14      |
| $\nu$ | Analytical | -0.0941                               | -0.2635 | -0.4451 | -0.5898 | 0.0439                                | -0.0942 | -0.2462 | -0.4095 |
|       | FEM        | -0.0767                               | -0.2524 | -0.4412 | -0.5923 | 0.0584                                | -0.0808 | -0.2353 | -0.4021 |

Finally, an analysis of equivalent (von-Mises) stress distribution on *i*2D-AS under vertical load was performed. The results for various parameters  $ah$  and  $bh$  are shown in Figs. 13 and 14, respectively. Due to the modified shape of the *i*-2D-AS compared to the original 2D-AS, there are fewer corners on the structure, so the possibility for the appearance of stress concentration regions is minimized.

The maximum values of the equivalent stress increase with the increase of parameters  $ah$  and  $bh$ , except when the value of parameter  $ah$  goes from 8mm to 12mm, where there is a slight drop in maximum values of equivalent stress.

**B: 8**  
Equivalent Stress  
Type: Equivalent (von-Mises) Stress  
Unit: MPa  
Time: 1  
11/6/2023 10:48 AM

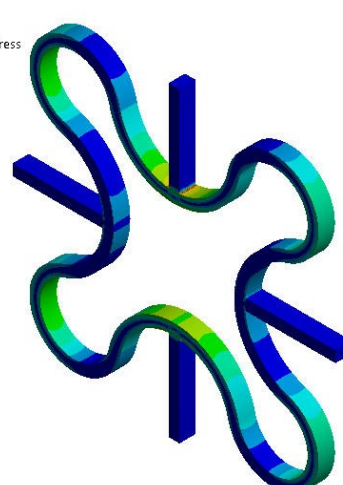
**16.852 Max**  
14.979  
13.107  
11.234  
9.362  
7.4896  
5.6172  
3.7448  
1.8724  
**1.6611e-12 Min**



(a)

**D: 12**  
Equivalent Stress  
Type: Equivalent (von-Mises) Stress  
Unit: MPa  
Time: 1  
11/6/2023 10:50 AM

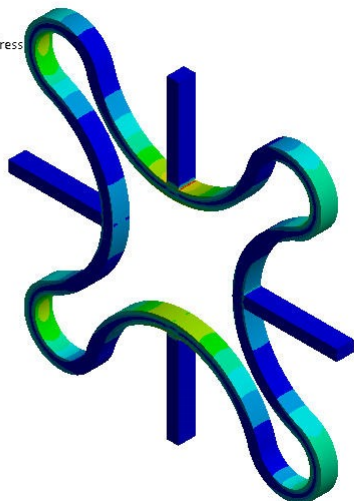
**16.131 Max**  
14.338  
12.546  
10.754  
8.9615  
7.1692  
5.3769  
3.5846  
1.7923  
**1.3826e-12 Min**



(b)

**G: 16**  
Equivalent Stress  
Type: Equivalent (von-Mises) Stress  
Unit: MPa  
Time: 1  
11/6/2023 10:51 AM

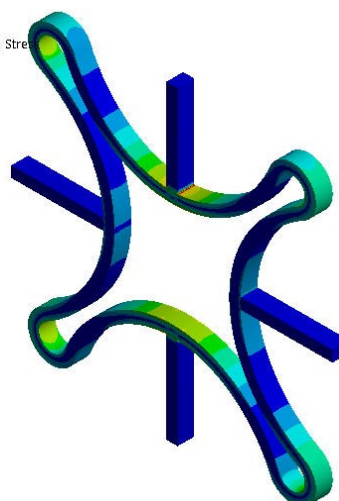
**16.855 Max**  
14.982  
13.11  
11.237  
9.364  
7.4912  
5.6184  
3.7456  
1.8728  
**1.8427e-12 Min**



(c)

**I: 20**  
Equivalent Stress  
Type: Equivalent (von-Mises) Stress  
Unit: MPa  
Time: 1  
11/6/2023 10:53 AM

**18.313 Max**  
16.278  
14.243  
12.209  
10.174  
8.1391  
6.1043  
4.0696  
2.0348  
**3.4548e-12 Min**

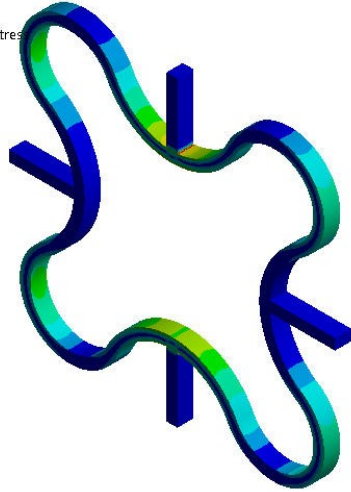


(d)

**Fig. 13.** Equivalent (von-Mises) stress distribution under the vertical load of *i*2D-AS for various values of parameter  $ah$  and  $bh=12.5$  mm: (a)  $ah=8$  mm, (b)  $ah=12$  mm, (c)  $ah=16$  mm, (d)  $ah=20$ mm.

**B: bh8**  
 Equivalent Stress  
 Type: Equivalent (von-Mises) Stress  
 Unit: MPa  
 Time: 1  
 11/6/2023 10:58 AM

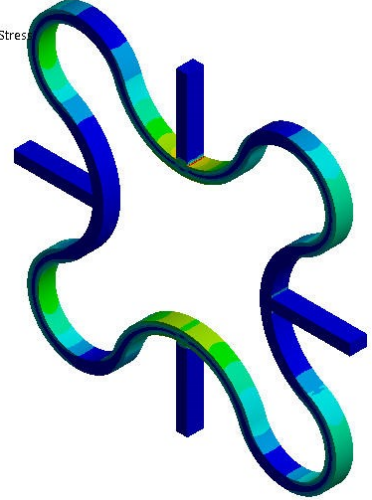
**15.845 Max**  
 14.084  
 12.324  
 10.563  
 8.8025  
 7.042  
 5.2815  
 3.521  
 1.7605  
**3.2967e-10 Min**



(a)

**C: bh10**  
 Equivalent Stress  
 Type: Equivalent (von-Mises) Stress  
 Unit: MPa  
 Time: 1  
 11/6/2023 11:00 AM

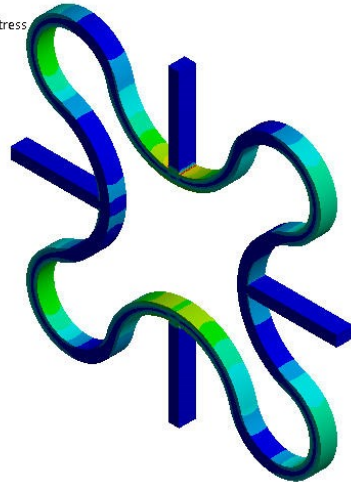
**15.992 Max**  
 14.215  
 12.438  
 10.661  
 8.8843  
 7.1074  
 5.3306  
 3.5537  
 1.7769  
**2.1142e-11 Min**



(b)

**D: bh12**  
 Equivalent Stress  
 Type: Equivalent (von-Mises) Stress  
 Unit: MPa  
 Time: 1  
 11/6/2023 11:01 AM

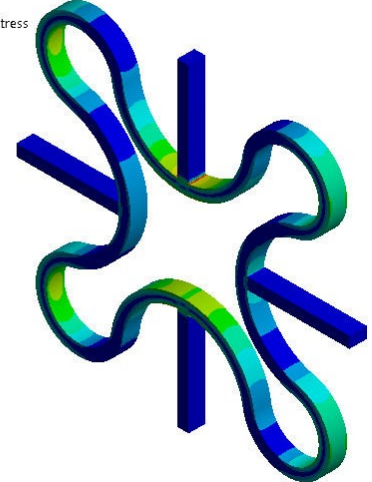
**16.099 Max**  
 14.31  
 12.521  
 10.732  
 8.9437  
 7.1549  
 5.3662  
 3.5775  
 1.7887  
**3.3783e-12 Min**



(c)

**E: bh14**  
 Equivalent Stress  
 Type: Equivalent (von-Mises) Stress  
 Unit: MPa  
 Time: 1  
 11/6/2023 11:03 AM

**16.165 Max**  
 14.369  
 12.572  
 10.776  
 8.9803  
 7.1843  
 5.3882  
 3.5921  
 1.7961  
**4.1678e-13 Min**



(d)

**Fig. 14.** Equivalent (von Mises) stress distribution under the vertical load of *i2D-AS* for various values of parameter *bh* and *ah*=12.5 mm: (a) *bh*=8 mm, (b) *bh*=10 mm, (c) *bh*=12 mm, (d) *bh*=14 mm.

### 3.3 Experimental verification

The specimens used for analysis in this study were produced using an EOS Formiga P100 machine (EOS GmbH, Krailling, Germany). The material used for specimen production was PA 2200, which is a polyamide 12. The laser-sintered specimens were produced from recycled powder mixed with 50% of new powder. The samples were manufactured using a 30 W power RF-excited CO<sub>2</sub> laser with 10.6  $\mu\text{m}$  wavelength and 254  $\mu\text{m}$  diameter of laser beam. The powder was preheated to 172°C, the laser beam power was 21 W, the laser scan speed was 2500 mm/s and the thickness of individual PA2200 layers was 100  $\mu\text{m}$ .

For experimental measurements, seven groups of the *i2D-AS* specimens with five replicas of each were produced. In the first four groups, the value of the parameter  $bh$  is fixed to 12.5 mm, while the parameter  $ah$  takes the values from 8mm to 20 mm with steps equal to 4 mm. In the last three groups the value of the parameter  $ah$  is fixed to 12.5 mm, while the parameter  $bh$  takes the values of 8 mm, 12 mm, and 16 mm. The other geometric parameters of the produced specimens are the same as in the previous numerical examples.

The experimental measurements were carried out by using the optical measurement technique on the ATOS COMPACT SCAN 5M scanner, as shown in Fig. 15. The camera was placed in the 300 mm position, while the measurement was performed by using a measuring volume of 300x230x230 mm. Previously, the scanner was calibrated according to the CP40/MV320 standard. Here, each of the structures was scanned twice, in the undeformed and deformed state.

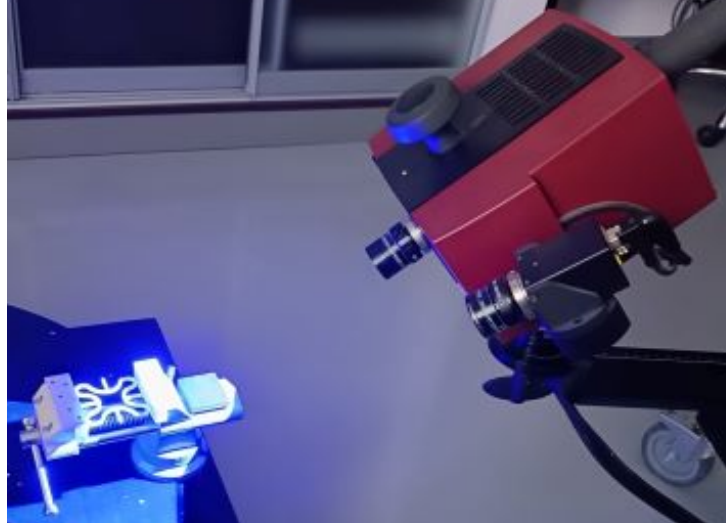


**Fig. 15.** The scanning process of *i2D-AS*

It's an idea to deform each of the specimens in the direction of the  $y$ -axis by using the clamp-on vise, as shown in Fig. 16. First of all, it is necessary to determine the exact dimensions  $L_x$  and  $L_y$  of the undeformed structure by scanning. After introducing an arbitrarily small displacement  $f_y$  in the vertical direction, by repeating the scanning process, we measure the quantities  $L'_x$  and  $L'_y$ .

Now, the values of the deformation of the specimen in the horizontal and vertical directions can be determined as:

$$f_x = L_x - L'_x, \quad f_y = L_y - L'_y. \quad (33)$$

Finally, the value of the Poisson's ratio should be obtained by using the expression (32).

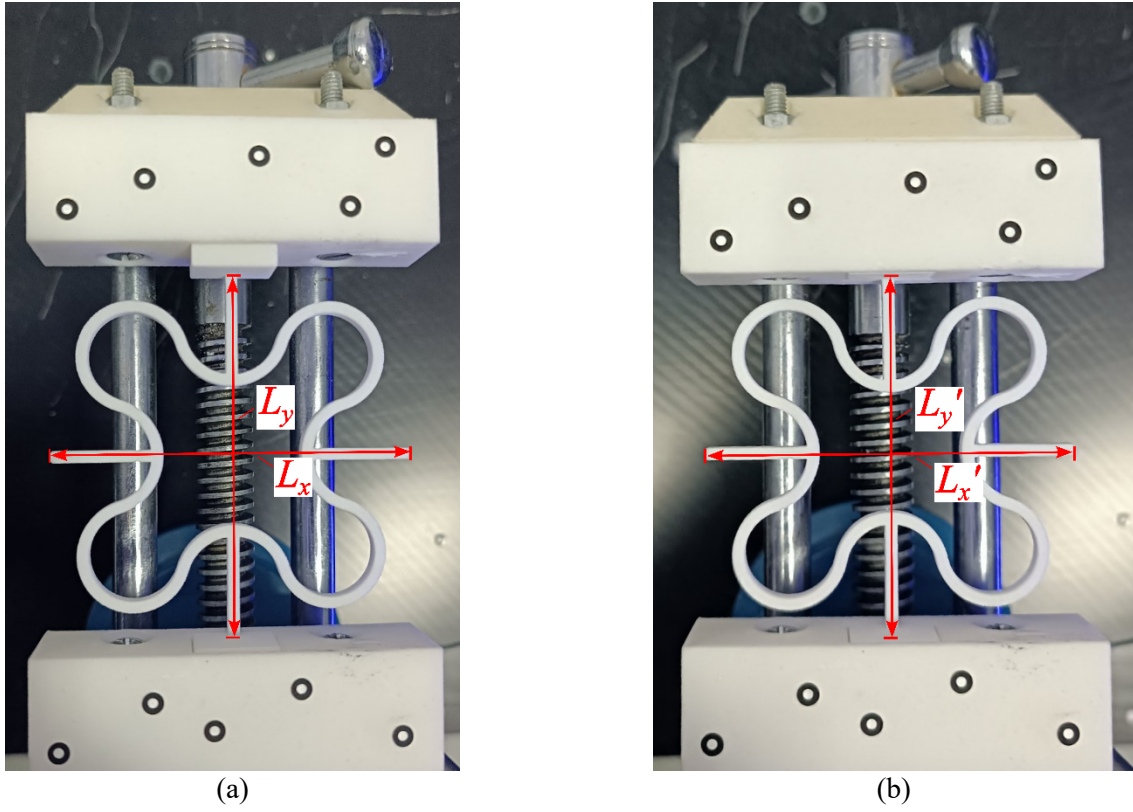


**Fig. 16.** The deformation process of *i2D-AS*: (a) undeformed, (b) deformed.

The example of the experimental results obtained by the measurements is shown in Fig. 17. First, Fig. 17(a) shows the scanned undeformed replica #1 of the specimen with parameters  $ah=8$  mm and  $bh=12.5$  mm, where the values of the parameters  $L_x$  and  $L_y$  can be read. Then, Fig. 17(b) shows the scanned deformed replica #1 of the same specimen from which the values of  $L'_x$  and  $L'_y$  are read. Applying expressions (32) and (33), Poisson's ratio of replica #1 of the considered specimen can be determined.



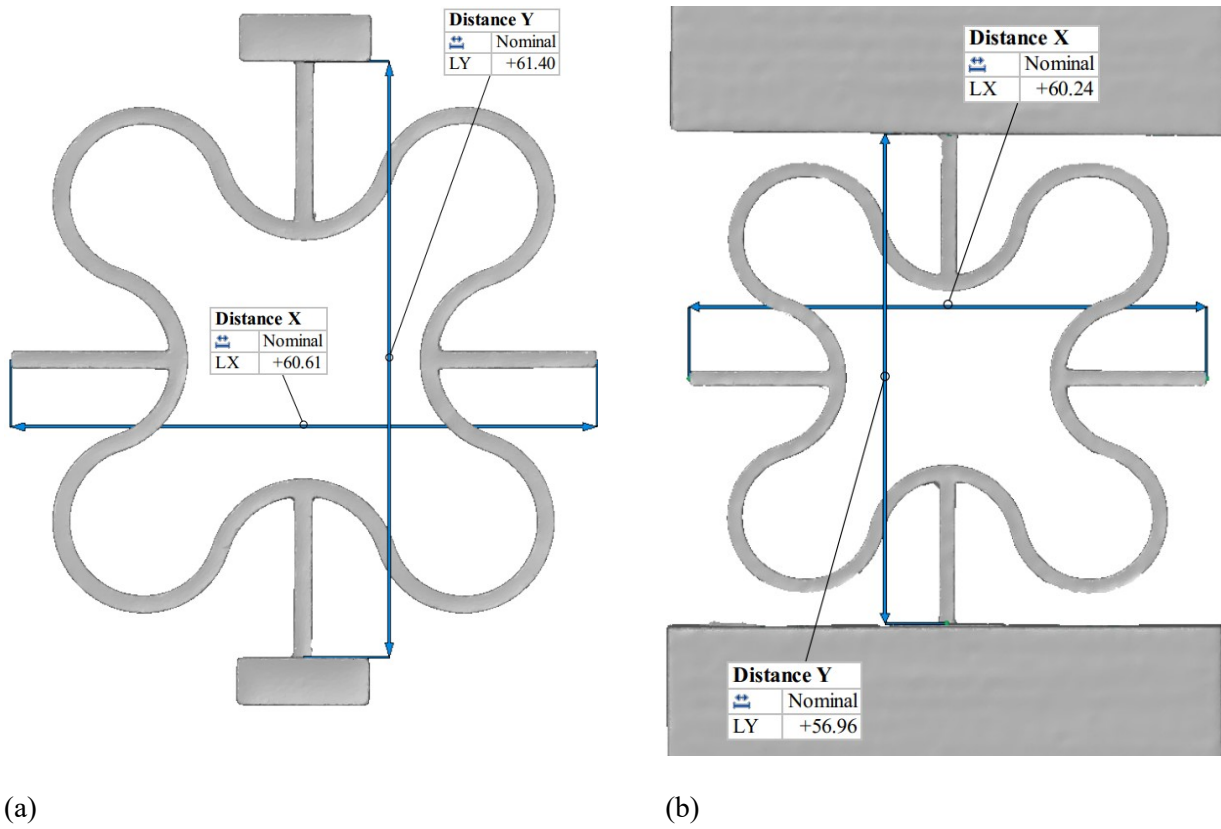


**Fig. 17.** The example of the scanned replica #1 of *i2D-AS* specimen for  $ah=8$  mm and  $bh=12.5$  mm: (a) undeformed, (b) deformed.

Table 5 contains the values of the Poisson's ratio  $\nu$  obtained by the procedure explained above. The values are obtained for all of the five measured replicas of each group of specimens. At the bottom of the table, the average values and standard deviation of the Poisson's ratio have been obtained. These average values of the Poisson's ratio will be used in the further analysis.



**Table 5**

The values of the Poisson's ratio  $\nu$  of *i2D-AS* obtained by the experimental measurement for various values of the parameters  $ah$  and  $bh$ .

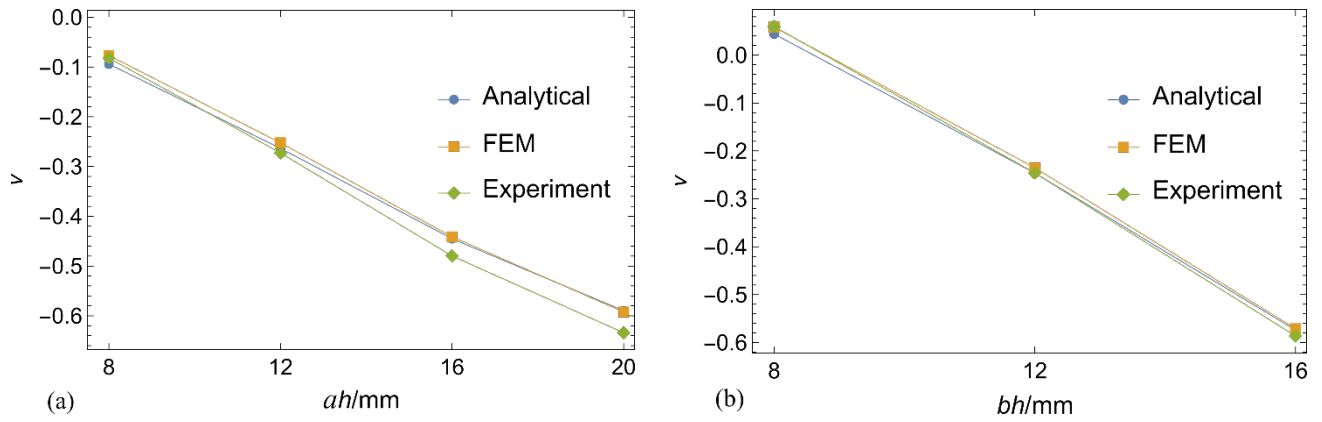
| Replica                    | $ah/\text{mm}$ ( $bh=12.5\text{mm}$ ) |                |                |                | $bh/\text{mm}$ ( $ah=12.5\text{mm}$ ) |                |                |
|----------------------------|---------------------------------------|----------------|----------------|----------------|---------------------------------------|----------------|----------------|
|                            | 8                                     | 12             | 16             | 20             | 8                                     | 12             | 16             |
| #1                         | -0.0844                               | -0.2553        | -0.4826        | -0.6254        | 0.0614                                | -0.2391        | -0.5982        |
| #2                         | -0.0722                               | -0.2762        | -0.4881        | -0.6468        | 0.0670                                | -0.2359        | -0.5978        |
| #3                         | -0.0852                               | -0.2824        | -0.4617        | -0.6387        | 0.0582                                | -0.2567        | -0.5872        |
| #4                         | -0.0830                               | -0.2754        | -0.4723        | -0.6184        | 0.0659                                | -0.2437        | -0.5709        |
| #5                         | -0.0849                               | -0.2747        | -0.4937        | -0.6411        | 0.0449                                | -0.2549        | -0.5772        |
| The average value of $\nu$ | <b>-0.0820</b>                        | <b>-0.2728</b> | <b>-0.4797</b> | <b>-0.6341</b> | <b>0.0595</b>                         | <b>-0.2461</b> | <b>-0.5863</b> |
| Standard deviation         | 0.0055                                | 0.0103         | 0.0128         | 0.0118         | 0.0089                                | 0.0093         | 0.0122         |

Table 6 shows the comparison of the values of the Poisson's ratio  $\nu$  obtained by using the analytical model, FEM as well as the experimental measurement for the various values of parameters  $ah$  and  $bh$ . A good match of the results from the above three sources can be observed. In the parentheses are given the relative errors of FEM and experimental results relative to analytical ones which are considered here as benchmark results. This error is within satisfactory limits when it comes to larger values of parameters  $ah$  or  $bh$ . Somewhat higher relative error values occur at  $ah=8\text{mm}$  and  $bh=8\text{ mm}$ . The assumption is that the reason for this is the very low values of Poisson's ratio, almost close to zero. Furthermore, a graphical representation of this comparison is given in Fig. 18 (a) and (b).

**Table 6**

The values of the Poisson's ratio  $\nu$  of *i*2D-AS obtained by the analytical model, FEM, and experimental measurement for various values of the parameters  $ah$  and  $bh$ .

| Method     | $ah/\text{mm} (bh=12.5\text{mm})$ |         |         |         | $bh/\text{mm} (ah=12.5\text{mm})$ |         |         |
|------------|-----------------------------------|---------|---------|---------|-----------------------------------|---------|---------|
|            | 8                                 | 12      | 16      | 20      | 8                                 | 12      | 16      |
| Analytical | -0.0941                           | -0.2635 | -0.4451 | -0.5898 | 0.0439                            | -0.2462 | -0.5738 |
| $\nu$ FEM  | -0.0767                           | -0.2524 | -0.4412 | -0.5923 | 0.0584                            | -0.2353 | -0.5710 |
|            | (18.49%)                          | (4.21%) | (0.88%) | (0.42%) | (33.03%)                          | (4.43%) | (0.49%) |
| Experiment | -0.0820                           | -0.2728 | -0.4797 | -0.6341 | 0.0595                            | -0.2461 | -0.5863 |
|            | (12.86%)                          | (3.53%) | (7.77%) | (7.51%) | (35.54%)                          | (0.04%) | (2.18%) |



**Fig. 18.** Comparison of the Poisson's ratio  $\nu$  of *i*2D-AS obtained by the analytical model, FEM, and experimental measurement: (a)  $bh=12.5\text{ mm}$ , (b)  $ah=12.5\text{ mm}$ .

## 4. Conclusions

In this paper, a detailed analytical model of the improved 2D arc-star structure was developed. It has been observed that for the same geometric parameters, a higher value of the NPR is obtained compared to the initial 2D arc-star structure [37] with the most often lower value of relative density, which directly leads to a lower consumption of the material. Also, the proposed analytical model was verified through checking with FEM as well as through measuring deformations on a real printed model using a 3D scanner. There is a good match of results from these three sources, which is what the analytical model is verified. This opens the door for further research regarding the optimization of geometric values or parameters of the structure material to maximize the value of the NPR of the structure which will be the subject of further research by the author in the future.

## Acknowledgment

This research was supported under grant no. 451-03-68/2022-14/200108 by the Ministry of Education, Science and Technological Development of the Republic of Serbia. This support is gratefully acknowledged.

## References

- [1] L.J. Gibson, M.F. Ashby, *Cellular Solids*, Cambridge University Press, 1997. <https://doi.org/10.1017/CBO9781139878326>.
- [2] T.-C. Lim, *Auxetic Materials and Structures*, Springer Singapore, 2015. <https://doi.org/10.1007/978-981-287-275-3>.
- [3] T.-C. Lim, *Mechanics of Metamaterials with Negative Parameters*, Springer Singapore, 2020. <https://doi.org/10.1007/978-981-15-6446-8>.
- [4] K.K. Saxena, R. Das, E.P. Calius, Three Decades of Auxetics Research – Materials with Negative Poisson’s Ratio: A Review, *Adv. Eng. Mater.* 18 (2016) 1847–1870. <https://doi.org/10.1002/adem.201600053>.
- [5] K.L. Alderson, A.P. Pickles, P.J. Neale, K.E. Evans, Auxetic polyethylene: The effect of a negative poisson’s ratio on hardness, *Acta Metall. et Mater.* 42 (1994) 2261–2266. [https://doi.org/10.1016/0956-7151\(94\)90304-2](https://doi.org/10.1016/0956-7151(94)90304-2).
- [6] I.G. Masters, K.E. Evans, Models for the elastic deformation of honeycombs, *Compos. Struct.* 35 (1996) 403–422. [https://doi.org/10.1016/S0263-8223\(96\)00054-2](https://doi.org/10.1016/S0263-8223(96)00054-2).
- [7] X. Zhang, R. Tian, Z. Zhang, G. Li, W. Feng, In-plane elasticity of a novel vertical strut combined re-entrant honeycomb structure with negative Poisson’s ratio, *Thin-Walled Struct.* 163 (2021) 107634. <https://doi.org/10.1016/j.tws.2021.107634>.
- [8] T. Baran, M. Öztürk, In-plane elasticity of a strengthened re-entrant honeycomb cell, *Eur. J. Mech. - A/Solids*. 83 (2020) 104037. <https://doi.org/10.1016/j.euromechsol.2020.104037>.

- [9] J. Shen, K. Liu, Q. Zeng, J. Ge, Z. Dong, J. Liang, Design and mechanical property studies of 3D re-entrant lattice auxetic structure, *Aerosp. Sci. Technol.* 118 (2021) 106998. <https://doi.org/10.1016/j.ast.2021.106998>.
- [10] A. Ingrole, A. Hao, R. Liang, Design and modeling of auxetic and hybrid honeycomb structures for in-plane property enhancement, *Mater. Des.* 117 (2017) 72–83. <https://doi.org/10.1016/j.matdes.2016.12.067>.
- [11] Y. Zhou, Y. Pan, L. Chen, Q. Gao, B. Sun, Mechanical behaviors of a novel auxetic honeycomb characterized by re-entrant combined-wall hierarchical substructures, *Mater. Res. Express.* 9 (2022) 115802. <https://doi.org/10.1088/2053-1591/ac9d83>.
- [12] F. Usta, H.S. Türkmen, F. Scarpa, High-velocity impact resistance of doubly curved sandwich panels with re-entrant honeycomb and foam core, *Int. J. Impact. Eng.* 165 (2022) 104230. <https://doi.org/10.1016/j.ijimpeng.2022.104230>.
- [13] H.H. Xu, H.C. Luo, X.G. Zhang, W. Jiang, X.C. Teng, W.Q. Chen, J. Yang, Y.M. Xie, X. Ren, Mechanical properties of aluminum foam filled re-entrant honeycomb with uniform and gradient designs, *Int. J. Mech. Sci.* 244 (2023) 108075. <https://doi.org/10.1016/j.ijmecsci.2022.108075>.
- [14] H. Wang, Z. Lu, Z. Yang, X. Li, A novel re-entrant auxetic honeycomb with enhanced in-plane impact resistance, *Compos. Struct.* 208 (2019) 758–770. <https://doi.org/10.1016/j.compstruct.2018.10.024>.
- [15] F. Jiang, S. Yang, C. Qi, H.-T. Liu, Two plateau characteristics of re-entrant auxetic honeycomb along concave direction, *Thin-Walled Struct.* 179 (2022) 109665. <https://doi.org/10.1016/j.tws.2022.109665>.
- [16] Z. Dong, Y. Li, T. Zhao, W. Wu, D. Xiao, J. Liang, Experimental and numerical studies on the compressive mechanical properties of the metallic auxetic reentrant honeycomb, *Mater. Des.* 182 (2019) 108036. <https://doi.org/10.1016/j.matdes.2019.108036>.
- [17] Y. Guo, J. Zhang, L. Chen, B. Du, H. Liu, L. Chen, W. Li, Y. Liu, Deformation behaviors and energy absorption of auxetic lattice cylindrical structures under axial crushing load, *Aerosp. Sci. Technol.* 98 (2020) 105662. <https://doi.org/10.1016/j.ast.2019.105662>.
- [18] X.C. Teng, X. Ren, Y. Zhang, W. Jiang, Y. Pan, X.G. Zhang, X.Y. Zhang, Y.M. Xie, A simple 3D re-entrant auxetic metamaterial with enhanced energy absorption, *Int. J. Mech. Sci.* 229 (2022) 107524. <https://doi.org/10.1016/j.ijmecsci.2022.107524>.
- [19] E. Harkati, N. Daoudi, A. Bezazi, A. Haddad, F. Scarpa, In-plane elasticity of a multi re-entrant auxetic honeycomb, *Compos. Struct.* 180 (2017) 130–139. <https://doi.org/10.1016/j.compstruct.2017.08.014>.
- [20] A. Harkati, D. Boutagoug, E. Harkati, A. Bezazi, F. Scarpa, M. Ouisse, In-plane elastic constants of a new curved cell walls honeycomb concept, *Thin-Walled Struct.* 149 (2020) 106613. <https://doi.org/10.1016/j.tws.2020.106613>.
- [21] Y. Chen, Z.-W. Wang, In-plane elasticity of the re-entrant auxetic hexagonal honeycomb with hollow-circle joint, *Aerosp. Sci. Technol.* 123 (2022) 107432. <https://doi.org/10.1016/j.ast.2022.107432>.
- [22] L. Shen, Z. Wang, X. Wang, K. Wei, Negative Poisson's ratio and effective Young's modulus of a vertex-based hierarchical re-entrant honeycomb structure, *Int. J. Mech. Sci.* 206 (2021) 106611. <https://doi.org/10.1016/j.ijmecsci.2021.106611>.
- [23] C. Zhan, M. Li, R. McCoy, L. Zhao, W. Lu, 3D printed hierarchical re-entrant honeycombs: Enhanced mechanical properties and the underlying deformation mechanisms, *Compos. Struct.* 290 (2022) 115550. <https://doi.org/10.1016/j.compstruct.2022.115550>.
- [24] F. Jiang, S. Yang, C. Qi, H.-T. Liu, A. Remennikov, L.-Z. Pei, Blast response and multi-objective optimization of graded re-entrant circular auxetic cored sandwich panels, *Compos. Struct.* 305 (2023) 116494. <https://doi.org/10.1016/j.compstruct.2022.116494>.
- [25] L. Wang, H.-T. Liu, Parameter optimization of bidirectional re-entrant auxetic honeycomb metamaterial based on genetic algorithm, *Compos. Struct.* 267 (2021) 113915. <https://doi.org/10.1016/j.compstruct.2021.113915>.

- [26] A. Álvarez-Trejo, E. Cuan-Urquizo, A. Roman-Flores, Effective Young's modulus of Bézier-based honeycombs: Semi-analytical modeling and the role of design parameters and curvature, *Thin-Walled Struct.* 192 (2023) 111136. <https://doi.org/10.1016/j.tws.2023.111136>.
- [27] Y. Zhu, S. Jiang, F. Lu, X. Ren, A novel enhanced anti-tetra-missing rib auxetic structure with tailorable in-plane mechanical properties, *Eng. Struct.* 262 (2022) 114399. <https://doi.org/10.1016/j.engstruct.2022.114399>.
- [28] H. Lu, X. Wang, T. Chen, Enhanced stiffness characteristic and anisotropic quasi-static compression properties of a negative Poisson's ratio mechanical metamaterial, *Thin-Walled Struct.* 179 (2022) 109757. <https://doi.org/10.1016/j.tws.2022.109757>.
- [29] W. Liu, Y. Zhang, Z. Guo, D. Li, S. Zhao, W. Xie, Analyzing in-plane mechanics of a novel honeycomb structure with zero Poisson's ratio, *Thin-Walled Struct.* 192 (2023) 111134. <https://doi.org/10.1016/j.tws.2023.111134>.
- [30] N. Xu, H.-T. Liu, M.-R. An, L. Wang, Novel 2D star-shaped honeycombs with enhanced effective Young's modulus and negative Poisson's ratio, *Extrem. Mech. Lett.* 43 (2021) 101164. <https://doi.org/10.1016/j.eml.2020.101164>.
- [31] Y. Zhao, Q. Zhang, Y. Li, B. Wang, F. Ma, Theoretical, emulation and experimental analysis on auxetic re-entrant octagonal honeycombs and its applications on pedestrian protection of engine hood, *Compos. Struct.* 260 (2021) 113534. <https://doi.org/10.1016/j.compstruct.2020.113534>.
- [32] H.-T. Liu, L. Wang, Design 3D improved star-shaped honeycomb with different tip angles from 2D analytical star-shaped model, *Compos. Struct.* 283 (2022) 115154. <https://doi.org/10.1016/j.compstruct.2021.115154>.
- [33] Y.-T. Jin, Y.-H. Qie, N.-N. Li, N.-W. Li, Study on elastic mechanical properties of novel 2D negative Poisson's ratio structure: Re-entrant hexagon nested with star-shaped structure, *Compos. Struct.* 301 (2022) 116065. <https://doi.org/10.1016/j.compstruct.2022.116065>.
- [34] W. Liu, H. Li, J. Zhang, X. Gong, Y. Wang, X. Ge, Tensile and shear properties of star-shaped cellular lattice structure, *Mech. Adv. Mater. Struct.* 28 (2021) 2605–2617. <https://doi.org/10.1080/15376494.2020.1747669>.
- [35] L. Ai, X.-L. Gao, An analytical model for star-shaped re-entrant lattice structures with the orthotropic symmetry and negative Poisson's ratios, *Int. J. Mech. Sci.* 145 (2018) 158–170. <https://doi.org/10.1016/j.ijmecsci.2018.06.027>.
- [36] X. Li, L. Gao, W. Zhou, Y. Wang, Y. Lu, Novel 2D metamaterials with negative Poisson's ratio and negative thermal expansion, *Extrem. Mech. Lett.* 30 (2019) 100498. <https://doi.org/10.1016/j.eml.2019.100498>.
- [37] Z.-Y. Zhang, J. Li, H.-T. Liu, Y.-B. Wang, Novel 2D arc-star-shaped structure with tunable Poisson's ratio and its 3D configurations, *Mater. Today Commun.* 30 (2022) 103016. <https://doi.org/10.1016/j.mtcomm.2021.103016>.